Ultramicroscopy 268 (2025) 114079

Contents lists available at ScienceDirect

Ultramicroscopy

journal homepage: www.elsevier.com/locate/ultramic

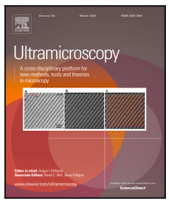

Direct electron detection for EBSD of low symmetry & beam sensitive ceramics

Nicolò M. Della Ventura [a,1], Andrew R. Ericks [a,1], McLean P. Echlin [a], Kalani Moore [b], Tresa M. Pollock [a], Matthew R. Begley [a], Frank W. Zok [a], Marc De Graef [c], Daniel S. Gianola [a,*]

[a] Materials Department, University of California Santa Barbara, Santa Barbara, CA, USA
[b] Direct Electron L.P., San Diego, CA, USA
[c] Department of Materials Science and Engineering, Carnegie Mellon University, Pittsburgh, PA, USA

ARTICLE INFO

Keywords:
Electron backscatter diffraction
Direct electron detection
Dictionary indexing
Ceramics
Beam sensitive materials

ABSTRACT

Electron backscatter diffraction (EBSD) is a powerful tool for determining the orientations of near-surface grains in engineering materials. However, many ceramics present challenges for routine EBSD data collection and indexing due to small grain sizes, high crack densities, beam and charge sensitivities, low crystal symmetries, and pseudo-symmetric pattern variants. Micro-cracked monoclinic hafnia, tetragonal hafnon, and hafnia/hafnon composites exhibit all such features, and are used in the present work to show the efficacy of a novel workflow based on a direct detecting EBSD sensor and a state-of-the-art pattern indexing approach. At 5 and 10 keV primary beam energies (where beam-induced damage and surface charge accumulation are minimal), the direct electron detector produces superior diffraction patterns with 10x lower doses compared to a phosphor-coupled indirect detector. Further, pseudo-symmetric variant-related indexing errors from a Hough-based approach (which account for at least 4%-14% of map areas) are easily resolved by dictionary indexing. In short, the workflow unlocks fundamentally new opportunities to characterize materials historically unsuited for EBSD.

1. Introduction

Few characterization techniques compare to electron backscatter diffraction (EBSD) in terms of speed and cost-effectiveness in determining the orientations, sizes, and shapes of grains with sub-micron resolution across millimeter length scales [1]. Many engineering and geological disciplines routinely leverage EBSD to, for example, characterize grain growth [2] and develop descriptions of elastic and plastic deformation [3,4]. However, unlike many metals, ceramics can be challenging to characterize due to one or more of the following features: small grain sizes, high crack densities, beam and charge sensitivities, low crystal symmetries, and pseudo-symmetric Kikuchi pattern variants. [5–7]. To this effect, progress in many application spaces is severely hampered by the inability to form new processing-structure–property connections across thermostructural [8–13], functional [14–21], tribological [22,23], and geological [24–28] ceramics (Fig. 1a).

Capturing EBSD information from ceramics presents numerous practical challenges that typically require low electron energies and doses. Small-grained samples require small electron beam interaction volumes and therefore low accelerating voltages, yielding weaker detector signals. Insulating ceramics require low electron doses (i.e. beam currents) to mitigate surface charge, which often results in image instability, brightness variations, astigmatism, beam drift, and variable beam interaction volumes. Charging can also be exacerbated on cracked specimens due to insufficient charge dissipation pathways. Also, the crystallinity of some ceramics degrades as the electron beam introduces defects, thereby amorphizing the material or inducing radiolysis [29–31]. Simply put, limiting electron dose and energy is often essential. Unfortunately, conventional phosphor-based EBSD detectors have a limited ability to capture weak signals (see Fig. 1b).

The scintillators in phosphor-based EBSD detectors present numerous challenges since the incident electron radiation must be converted to photons, then transmitted via fiber optics to a photodetector. The fundamental energy-dependent inefficiencies, rooted in the underlying physics of the detection process, are difficult to overcome particularly at low accelerating voltages and manifest as low signal-to-noise ratios (SNR), poor quantum efficiency, a poor point-spread function, decreased spatial resolution, limited acquisition speeds and reduced sensitivity to weak signals. These drawbacks are especially problematic for time-resolved *in situ* experiments.

* Corresponding author.
E-mail address: gianola@ucsb.edu (D.S. Gianola).
[1] These authors contributed equally to this work

https://doi.org/10.1016/j.ultramic.2024.114079
Received 22 June 2024; Received in revised form 5 October 2024; Accepted 14 November 2024
Available online 23 November 2024

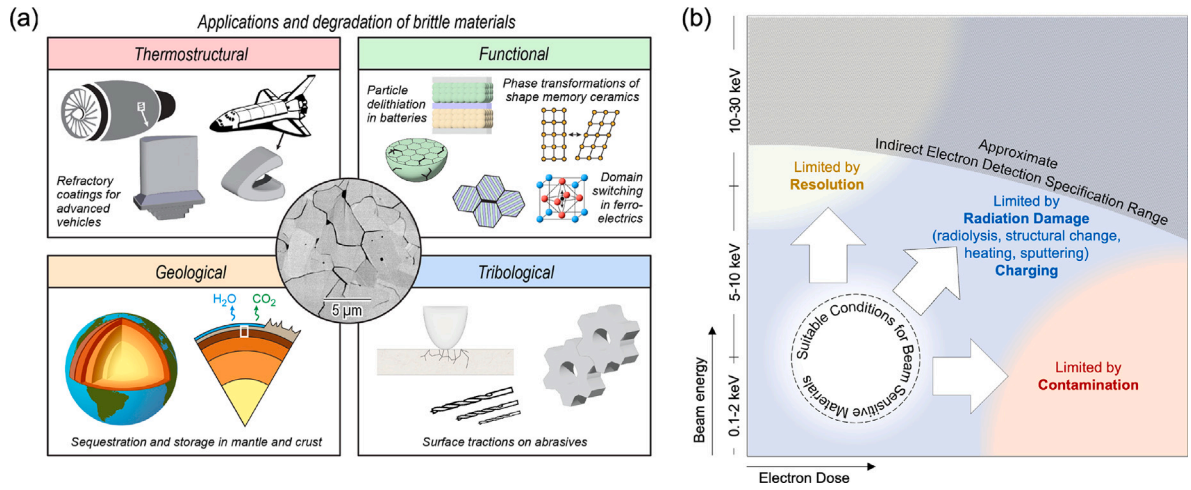

Fig. 1. (a) Four application spaces in which grain boundary microcracking compromises the properties and mechanical integrity of brittle materials. The central inset features a backscattered electron (BSE) image of monoclinic hafnia. Materials with high thermoelastic anisotropy may crack at small grain sizes, thereby making EBSD characterization difficult or infeasible. These microcracked beam-sensitive materials limit the range of practicable beam energies and electron doses for EBSD data acquisition. A qualitative representation of these challenges is shown in (b). The vertical axis shows that the spatial resolution of patterns degrades at high accelerating voltages for small-grained materials. High voltages coupled with high electron doses can lead to problems including sample radiolysis. The scintillator-free (direct) EBSD detector mitigates these issues by enabling the use of low primary beam energies and doses while preserving details of higher-order Kikuchi diffraction information. Wikimedia image credit: Illustrations of Space Shuttles, Earth's layers by Mats Halldin.

In contrast to phosphor-based indirect detectors, recently developed silicon-based, scintillator-free, direct detectors for EBSD allow for the fast capture of high resolution diffraction patterns [32] with enhanced electron sensitivity [33–35] at low accelerating voltage and electron dose (Fig. 1b). Critically, the Kikuchi patterns from direct detection are rich in higher-order diffraction information, and thus the sharply resolved patterns present new opportunities to quickly and accurately characterize materials that are typically unsuited for EBSD. In this work, to demonstrate this potential, we focus on two such materials: monoclinic hafnia and tetragonal hafnon.

Monoclinic hafnia (HfO_2, space group $P2_1/c$, point group 2/m) is stable up to ~1800 °C and is a candidate for thermal/environmental barrier coatings and ultra-high temperature coatings [13,36–43]. However, its high thermal expansion anisotropy [44–46] typically precludes its use in monolithic form because when the grains exceed ~2-3 μm, the grain boundaries crack [42,43,47]. Tetragonal hafnon ($HfSiO_4$, $I4_1/amd$, 4/mmm), has several attractive qualities that make it complementary to hafnia. Namely, hafnon is stable in contact with hafnia to high temperatures (~1600 °C) and it exhibits much lower thermoelastic anisotropy than hafnia [48,49]. Its critical grain size for cracking is likely at least a factor of 10-100x larger than that of hafnia [43]. Recent work has demonstrated that dispersing hafnon in hafnia/hafnon composites yields dense, crack-free specimens [43]. While the composites are readily fabricated using conventional ceramics processing techniques, electron backscatter pattern (EBSP) acquisition and indexing is challenging with indirect phosphor detectors and Hough-based indexing approaches; the microstructures, beam sensitivities, and pseudo-symmetric (PS) variants necessitate alternative workflows to enable accurate pattern indexing [6].

EBSP indexing algorithms are crucial to accurately identify grain orientations, especially for materials of low crystal symmetry. New indexing approaches continue to emerge, including Hough transform-based algorithms [50–53], forward model driven dictionary indexing and spherical harmonics-based pattern matching [54–61], and Radon-transform-based algorithms [62]. The inherent trade-off between high throughput and accuracy means that fast algorithms sometimes compromise indexing fidelity, while slower algorithms may be more accurate but lead to longer compute times. The latter are often necessary for indexing materials of low symmetry with numerous pseudo-symmetric (PS) variants, such as hafnia. Irrespective of the approach, a key first step to indexing is to determine the geometric parameters that describe the spatial relationships between the electron source, sample, and detector.

The most difficult to define of the geometric parameters is the pattern center (PC), which is the point on the detector from which a normal vector is incident on the diffracting location at the sample surface. Examples of approaches that can simultaneously fit both pattern center and an indexed orientation include the global optimization method [63], the strain minimization technique integrated into the open-source HR-EBSD package OpenXY [64], the differential evolution global optimization algorithm [65], the optimization routines in the dictionary indexing software EMsoft [59], among others [53,66]. Accurate PCs are critical to the efficacy of the indexing algorithm, and especially so for low symmetry materials exhibiting many PS variants [6,7,67]. In the present work we demonstrate that the workflow is procedurally flexible in that the position of the detector can be adjusted to tailor the solid angle for EBSP acquisition; the approach naturally requires easy and accurate PC determination.

This article is organized as follows. Section 2 describes the material fabrication, data collection, and data processing methods. Section 3 presents two parametric studies; the first compares the performance of a DE-SEMCam camera to a conventional indirect EBSD detector in order to highlight the considerable differences in electron sensitivity and resulting patterns. The second compares the Hough indexing (HI) and DI approaches to characterize the grain structures of hafnia/hafnon specimens and to quantify the accuracy with which the indexing techniques handle PS variants. Section 4 provides a forward-looking discussion on opportunities for future work, and Section 5 summarizes key conclusions.

2. Methods

2.1. Materials and processing

Materials used in the current study comprise sintered pellets of monolithic hafnia, monolithic hafnon, and composites of 50 vol% of each of the constituent materials. Hafnia powder (99% metals basis, excluding Zr, Alfa Aesar, Ward Hill, MA) and hafnon powder (provided by an industry collaborator) were used to make the pellets. Details of the feedstock powders and pellet fabrication are described elsewhere [43]. Briefly, 10 mm diameter cylindrical pellets were prepared using field-assisted sintering (FAST, FCT Systeme GmbH, Frankenblick,

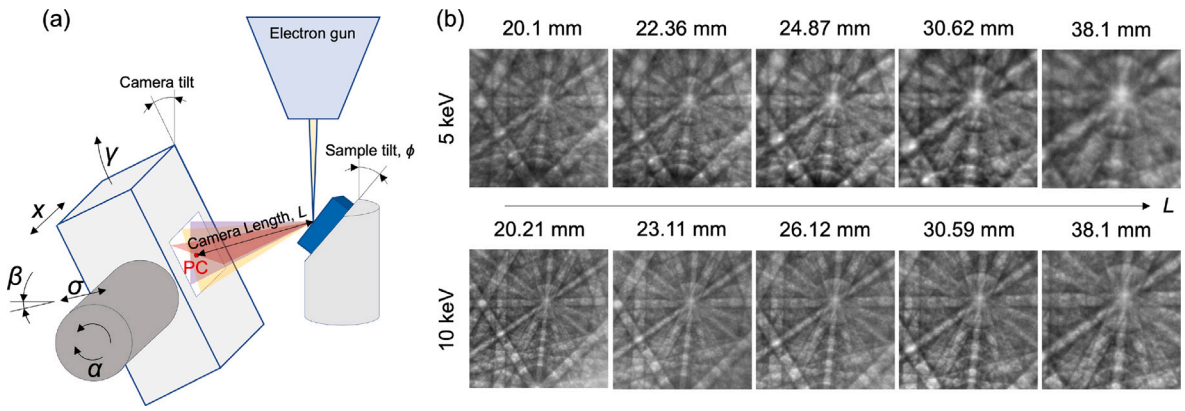

Fig. 2. (a) Schematic showing the pertinent geometric parameters for EBSD data collection. In the DE-SEMCam, an external, manually operated mechanical positioning system, as described in Wang et al. [32], offers translational and rotational control of the detector within the SEM chamber. (b) EBSPs of hafnia captured with the DE-SEMCam at various keV and camera lengths, denoted as *L*. The smallest and largest *L* values are 20.1 and 38.1 mm, respectively, corresponding to solid angles of 67° and 38.5°. At a constant *L*, reducing the keV results in broader Kikuchi band widths.

Germany) [68]. For the composites, dry powders were first mixed in the appropriate amounts and suspended in a H_2O-NH_4OH_4 solution of pH 11 and agglomerates were broken up using an ultrasonic horn. The powders were dried at 80 °C for 12 h, ground using a mortar and pestle, and sintered for 16 min at 1650 °C and 100 MPa using heating and cooling rates of 150 °C min^{-1}. For the pure hafnia and pure hafnon pellets, dry powders were loaded into the FAST die sets and sintered for 16 min at 1400 °C or 64 min at 1650 °C, respectively, with pressures of 100 MPa and heating and cooling rates of 150 °C min^{-1}. These parameters were chosen to ensure that the grain sizes of the three types of samples were comparable Previous experience with similar processing conditions indicates that the pellets were 97%–99% dense (ASTM C373) [69].

To prepare for EBSD data acquisition, sintered pellets were sectioned along their diametral mid-planes and polished to a 0.25 μm finish using SiC paper and colloidal diamond suspension followed by ion milling with broad Ar beams (Leica EM TIC 2X, 2–8 keV). The surface of the monolithic hafnia sample was coated with a thin layer (ca. <5 nm) of sputtered carbon to mitigate surface charging resulting from extremely high density of cracks in this sample. Neither the hafnon or hafnia/hafnon composite samples required any conductive coating.

2.2. EBSD acquisition

EBSD was carried out using the DE-SEMCam manufactured by Direct Electron LP (San Diego, CA), equipped with a custom monolithic active pixel sensor (MAPS, full-frame resolution 4096 × 4096, 2x hardware binning 2048 × 2048, effective pixel size of 13 μm, maximum readout speed 281 fps) [32], and the TSL/EDAX EBSD Hikari Plus (full-frame resolution 640 × 480 and effective pixel size of 67.5 μm) detector. The DE-SEMCam was installed on a Thermo Fisher Scientific Apreo-S scanning electron microscope (SEM) and the latter on a Thermo Fisher Scientific Versa 3D SEM. Both microscopes were operated at accelerating voltages of 5 and 10 keV. The EBSPs were dark- and flat field-background subtracted. Dark reference backgrounds were collected with the detector in position in the chamber with the electron beam blanked and all photon sources inactive. Background images were calculated as the average of all the patterns collected from the hundreds to thousands of grains present in each acquisition area.

2.3. Geometry of EBSD setup

EBSP of hafnia were collected from an identical sample location at various camera lengths (*L*) for both 5 and 10 keV using the DE-SEMCam detector (Fig. 2b). Sample tilt corresponds to 70°. Camera lengths were determined from an optimized pattern center at each detector distance. Pattern centers (PC: x^*, y^*, z^*) were defined by comparing each experimental EBSP to simulated patterns from the dynamical master pattern (Fig. 3, described in Section 2.4) via a gnomonic projection using the Efit program in EMsoft [70]. Additional details on the PC determination are described in the Supplementary Materials section B.

The camera length is defined as:

$$L = z^* N_x^s \delta \tag{1}$$

where δ is the detector pixel size (with binning, if any), and N_x^s, N_y^s are the number of pixels of size δ (upon binning) that define the detector width and height. Here, $N_x^s \times \delta = 104\,\mu m \times 256\,pxl = 26.624\,mm$. Based on the size of the DE-SEMCam sensor, one can then compute the solid angle coverage for each pattern using:

$$Solid\,Angle \simeq 2\arctan\left(\frac{N_y^s \delta}{2}\frac{1}{L}\right) \tag{2}$$

In Fig. 2b, the DE-SEMCam detector distance is varied over a distance of 18 mm, from 20.1 mm to 38.1 mm, to modify the angular resolution per pixel. This equates to a range in solid angle of ~28.5°, from 67° to 38.5° (i.e., 0.03°/px and 0.019°/px). Hereafter, all of the DE-SEMCam EBSD datasets used camera lengths between 23 mm to 27 mm. We anticipate that, for monoclinic hafnia in particular, indexing was greatly improved when the detector covered more diffraction space at shorter camera lengths.

2.4. EBSP indexing

EBSPs were indexed using Hough and dictionary techniques. Briefly, HI transforms the spatial relationships of Kikuchi bands into a new parameter space, where these relationships are compared to a list of angles between high intensity diffracting planes derived from a reference crystal structure. As will be shown, the approach can struggle with low symmetry crystals and noisy patterns collected at low beam voltages. The HI parameters are given in Table A.1 and were employed using the EDAX OIM v9 software.

The DI method is different in that it compares experimental patterns to a library of simulated diffraction patterns, each representing a unique orientation, using the normalized dot product as a similarity metric. The orientation with the highest normalized dot product match is assigned to the experimental pattern. Afterwards, a refinement step is applied that searches for the ideal orientation solution around the closest dictionary solution. For the composite samples, the entire dataset is processed using each phase individually before a refinement step in which the final phase selection is determined on a point-by-point basis using the highest normalized dot product. The simulated EBSPs are generated using a two-step physics-based forward model that: (1)

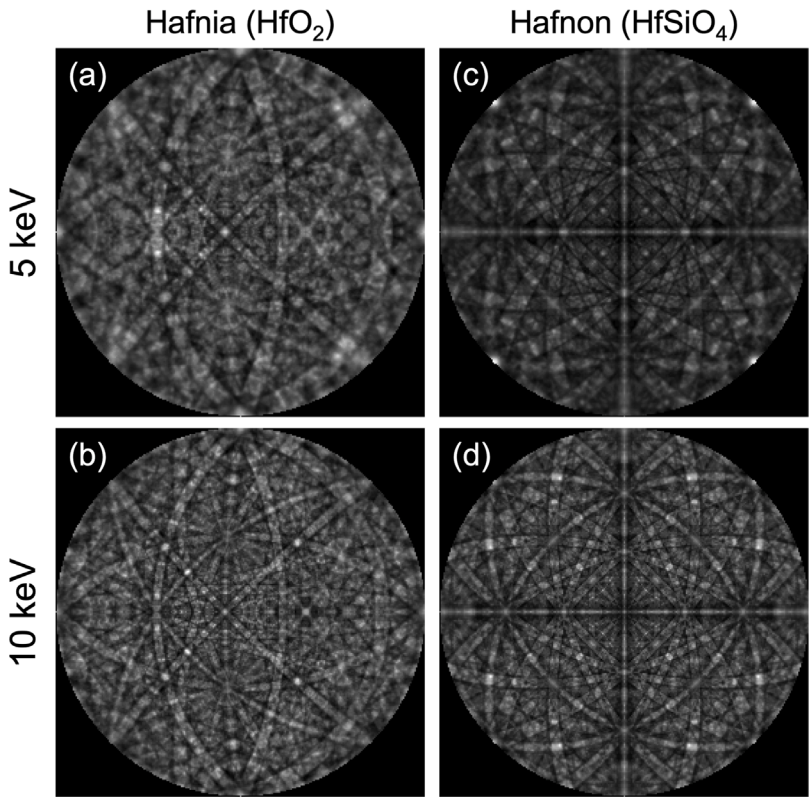

Fig. 3. Stereographic projection of the simulated master patterns for hafnia (a,b) and hafnon (c,d) at 5 and 10 keV obtained using the open-source software EMsoft [71].

computes backscatter yield via a Monte Carlo simulation on the Kikuchi sphere and then (2) uses a quantum mechanical model to calculate the diffracting electron intensities as they exit the sample. The resulting intensity distributions, known as master patterns (MP), are sampled using gnomonic projections, which account for the sample and detector geometries, to generate a dictionary of simulated EBSD patterns across all orientation space. This dictionary of simulated patterns is then compared to each experimental pattern using a similarity metric (maximum dot product), to determine the best match. EMsoft v6.0 [71] was used to generate the MPs for hafnia and hafnon at 5 and 10 keV, which are shown in Fig. 3. Excellent resources on the DI method are included here [55,59,72,73].

Pattern centers were determined by hand using the Efit software in EMsoft for all EBSD datasets in this work. Furthermore, for comparisons between HI and DI, the exact same pattern centers (see Table A.3) were used to index the datasets.

The MPs are useful for identifying PS variants, which arise when multiple crystal orientations that are not related by symmetry operations give rise to nearly indistinguishable EBSPs due to the limited solid angle of the detector [5]. Some of the most prevalent PS variants for hafnia and hafnon are given in Table A.4, calculated by correlating each MP to itself using the spherical indexing approach [5]. The auto-correlation intensity estimates the likely PS variants vis-á-vis their relative misorientation. At the maximum auto-correlation value of 100, we see the MP aligned (also accounting for symmetrically equivalent variants) with no misorientation from the reference MP (itself). All values near and below 100 are misorientations that likely result in PS variants. The statistical prevalence for any specific PS variant, defined by direction, plane, and angle, is that for a 'best-case scenario' since the auto-correlation procedure considers the full 4π solid angle of the Kikuchi sphere (entire MP). In practice, real detectors with smaller solid angles further increase the likelihood of PS confusion since only a subset of the full Kikuchi sphere is imaged.

In the present work, we assume that hafnia twin boundaries correspond to disorientations of ~180°, given their considerable over-representation compared to the theoretical orientation distribution function in Fig. 7c,d. To our knowledge, there are no available works dedicated to thoroughly characterizing multiple twin boundaries in monoclinic hafnia and, admittedly, twins of other disorientations could exist. It is encouraging, though, that twin boundaries have been observed within hafnia grains by scanning transmission electron microscopy [43], forming domains qualitatively similar to the ones in the present work.

3. Results

The first of the two parametric studies compares the EBSP quality of hafnia obtained from the indirect and direct detectors at low accelerating voltages. Detection parameters are presented in Table A.2 and discussed in Section 3.1. The second study (Section 3.2–3.3) uses the direct detector EBSD data to compare the accuracy of HI to DI for hafnia, hafnon, and hafnia/hafnon composites. High resolution maps, presented in Section 3.4 are used to elucidate microstructural features, reveal the origins of indexing errors, and quantify the effects of PS variants on pattern quality.

3.1. Comparison of detector sensitivity

To compare the sensitivity of the two detectors, single EBSPs corresponding to similar grain orientations of hafnia were collected at 5 keV and 10 keV following optimization of the electron beam current, camera binning, exposure time, and gain. The results for both detectors are shown in Fig. 4. Those corresponding to the indirect detector (a,b) were selected from the top 25% confidence index values in the dataset although visual inspection revealed that most patterns contained little diffraction information. While the primary diffraction bands are visible in the 10 keV pattern (b), none are discernible in the 5 keV pattern (a).

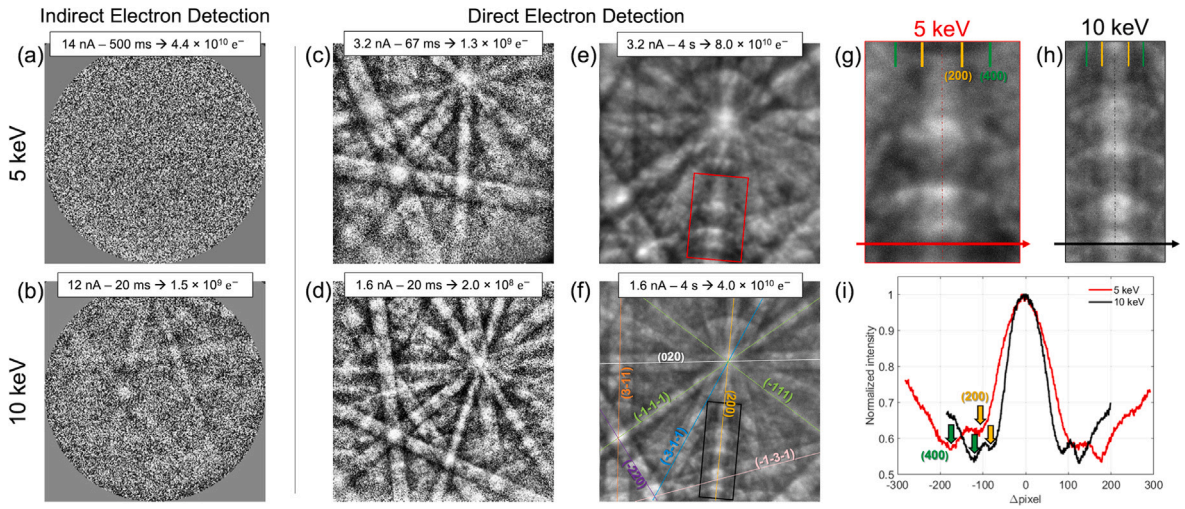

Fig. 4. Hafnia EBSPs from fixed sample locations using indirect and direct electron detectors. (a,b) EBSPs from the TSL/EDAX detector at 5 and 10 keV. (c,d) EBSPs from the DE-SEMCam detector at 5 and 10 keV. Even at lower relative electron doses the DE-SEMCam detector collects higher quality EBSPs than the indirect TSL/EDAX detector. (e,f) EBSPs acquired at longer times reveal fine diffraction details, with enlarged sections (g,h) showing higher-order bands. Flat fielding/background subtraction (computed as the average of all patterns in each map) were applied to all EBSPs. The electron dose reported above each EBSP is determined using Eq. (3). Note that the camera length, L, in (c,d) is lower than (a,b), whilst in (e,f) is higher than (a,b) - see Table A.2: the number of electrons per unit area varies following a $1/L^2$ dependence.(i) Integrated line profiles extracted from (g,h) across the (200) Kikuchi band.

Inverse pole figure (IPF) maps of the full EBSD datasets collected with the indirect detector are depicted in the Supplementary Information (Figure S2), and were processed using HI in EDAX OIM v9.

In stark contrast, the direct detector captures higher-order diffraction information for both beam conditions shown in Fig. 4c,d. Although the optimal electron sensitivity for this detector has been found to correspond to accelerating voltages of 10–18 keV [32], the collection efficiency is evidently still good for the direct detector at 5 keV. What is more, the direct detector outperforms the indirect detector at shorter exposure times (and therefore lower electron doses); the acquisition parameters listed in Table A.2 provide a means to estimate the effective electron dose per EBSP, given as:

$$N_{electrons} = \frac{I \times \Delta t}{q} \tag{3}$$

where I is the beam current, Δt is the exposure time, and q is the electron charge (1.602×10^{-19} C). The electron doses for the indirect detector (Fig. 4a,b) are 34 and 7.5 times higher than those for the direct detector (Fig. 4c,d) at equivalent voltages.

Fig. 4e,f illustrates how the EBSP quality and diffraction information, such as high-order bands, can be further enhanced by extending both exposure times and camera lengths at each voltage. While increasing exposure time alone would result in approximately twice the electron dose in panel (e) compared to the indirect detector in panel (a), as described by Eq. (3), it is important to note that a greater detector distance not only enhances the angular resolution in diffraction space but also reduces the number of electrons per unit area by $1/L^2$, further highlighting the importance of employing high-sensitivity detectors for high angular resolution studies.

Fig. 4g,h presents higher magnification images of the EBSPs from (e,f). Integration across the bands, indicated by the red and black arrows in (g) and (h) respectively, demonstrates the detectability of the (200) and (400) reflections (Fig. 4i). Since bands broaden as voltage decreases, the bands corresponding to 5 keV (g) span more pixels than those for 10 keV (h) for a fixed camera length.

We emphasize that the phosphor-based CCD (Charge-Coupled Device) camera employed in this work, renowned for its high performance in HR-EBSD [74], is utilized as a benchmark to contextualize our findings. Notable advancements in CMOS (Complementary Metal-Oxide-Semiconductor) technology over conventional CCD detectors have been demonstrated, particularly in facilitating rapid pattern acquisition through enhanced read-out electronics. CMOS-based systems have shown considerable improvements in low signal-to-noise ratio patterns via pattern averaging, achieving precision comparable to CCD detectors while reducing acquisition times by a factor of up to three [74]. Despite technological advancements and refinements in phosphor-based (indirect) detection systems, a significant loss of sensitivity occurs due to phosphor-coupling, regardless of the accelerating voltage. This loss is an intrinsic limitation dictated by the physics of the detection process. Furthermore, the energy-dependent nature of this inefficiency becomes particularly pronounced with decreasing primary beam energies, as photon generation efficiency declines, exacerbating the problem. This is especially evident at low accelerating voltages, where direct electron detectors exhibit superior performance, as demonstrated by the results shown here.

3.2. Comparison of indexing approaches using Hafnia and direct electron detection

Here, the focus turns to comparing Hough and dictionary indexing. EBSD maps of hafnia collected by the DE-SEMCam were indexed using both techniques to produce the IPF maps in Fig. 5. At 5 keV, HI produces noisy maps with multiple orientations within essentially all of the grains (Fig. 5a) while DI performs better (Fig. 5b). Increasing the accelerating voltage to 10 keV reduces the indexing errors from the Hough transform (Fig. 5c,d), but high magnification sub-regions reveal that DI better resolves subtle features like twin boundaries (Fig. 5e,f). Panels (e,f) also show that HI produces errors with significant angular deviations (black circles on IPF legend) as well as different parent-twin (P-T) relationships compared to DI (green and blue points on IPF legend).

3.3. EBSD of Hafnon and composite specimens

EBSD scans were collected at 10 keV from pure hafnon and the hafnia/hafnon composite and then indexed using DI (HI results are reported in Supplementary Figure S3). The detection parameters are reported in Table A.3. The IPF and image quality maps, together with those for pure hafnia, are shown in Fig. 6. The high quality of the maps enables quantification of microstructural features including grain size and shape; the average grain size in pure hafnia is ~ 1.49 μm while that in pure hafnon is ~0.37 μm. There are also many twin boundaries

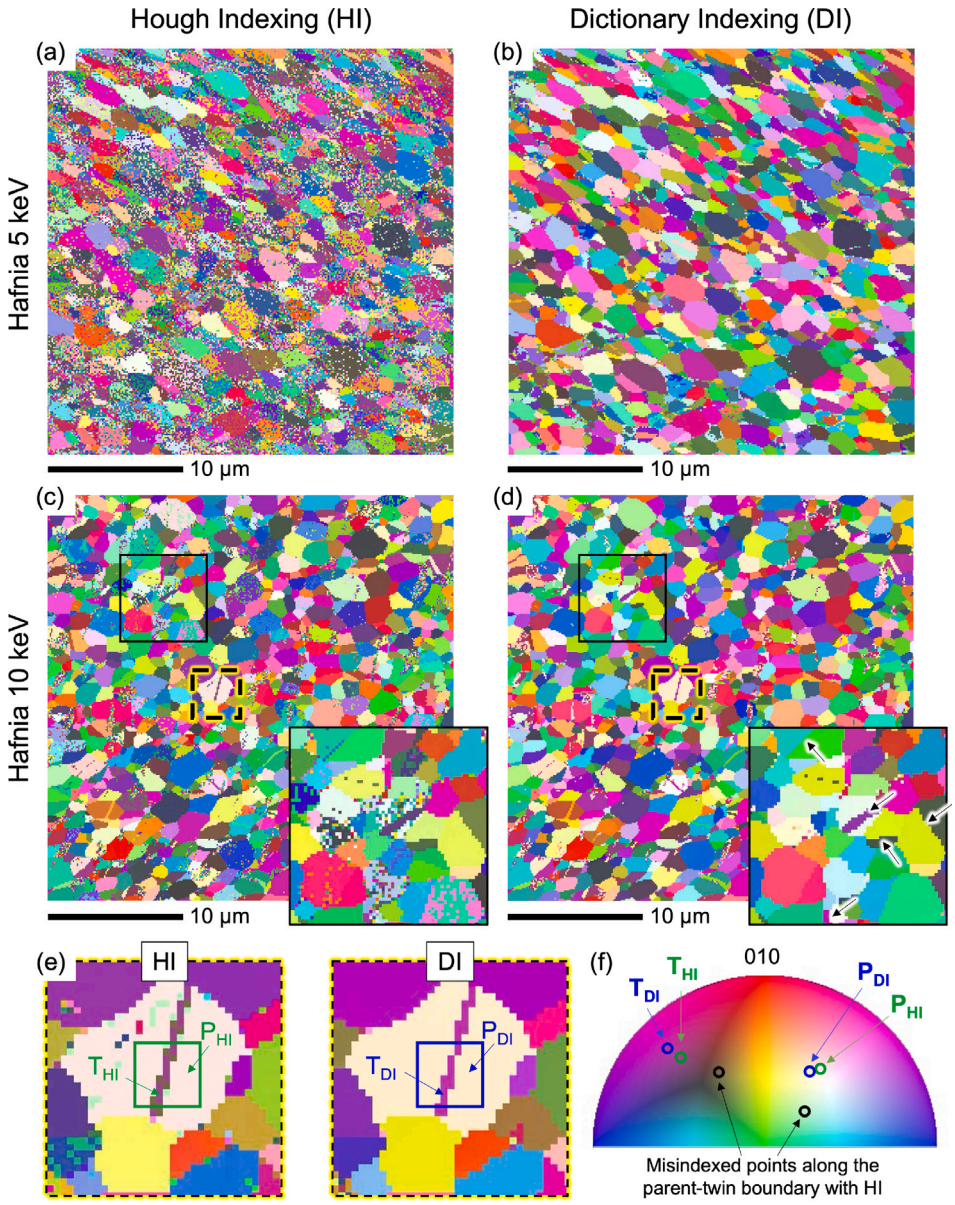

Fig. 5. EBSD maps of hafnia following HI or DI at (a,b) 5 keV and (c,d) 10 keV, collected using the DE-SEMCam and indexed using the same pattern center values. Maps in (a,b) are for the same region, just as in (c,d). DI successfully indexes more points than HI, especially for the 5 keV dataset. Insets in (c) and (d), denoted by solid outlines, show that DI resolves micron-scale features. Panels (e,f), corresponding to the dashed outlines in (c,d), reveal subtle yet important differences in indexed orientations along a twin boundary.

in hafnia (Fig. 6d) but not in hafnon. This aligns with the composite map (Fig. 6f) in that only hafnia grains exhibit twins; the twins in the composite account for ~37% of all grain boundaries, which is about three times that in pure hafnia (~11.1%). It is encouraging that the direct detection EBSD-DI workflow is capable of resolving multiple high-aspect-ratio twin domains within the small hafnia grains in the composite.

3.4. Error quantification between indexing approaches

We next compare the indexing methods using hafnia. Fig. 7a,b presents the disorientation maps derived from point-to-point comparisons of the same scans indexed with HI and DI, and Fig. 7c,d shows the corresponding histograms. A disorientation is the smallest possible rotation angle required to align one crystal with another, out of all symmetrically equivalent rotations. The disorientations are attributable to several factors. First, both indexing approaches generate random errors in which one or both algorithms fail to properly index an EBSP; the disorientation values across all EBSPs (pixels) give rise to a population reminiscent of the well-known orientation distribution function (i.e. Mackenzie distribution), reflecting the statistical distribution of crystal orientations in an aggregate of randomly oriented crystals of the same symmetry [76].

Random indexing errors do not, however, account for all of the disorientations. Many are below 20° and above 176°, as shown by both histograms in Fig. 7c,d. The small disorientations indicate errors in solutions specific to the indexing algorithms; the lowest disorientation in the 5 keV map is 3.48° while that for the 10 keV map is 0.02°, The disorientations above 176° reflect another source of error: PS variants. Potential hafnia PS variants are shown in Table A.4, calculated by correlating the MP to itself using the spherical indexing technique [5]. For hafnia, the angular deviation between ambiguous orientations is

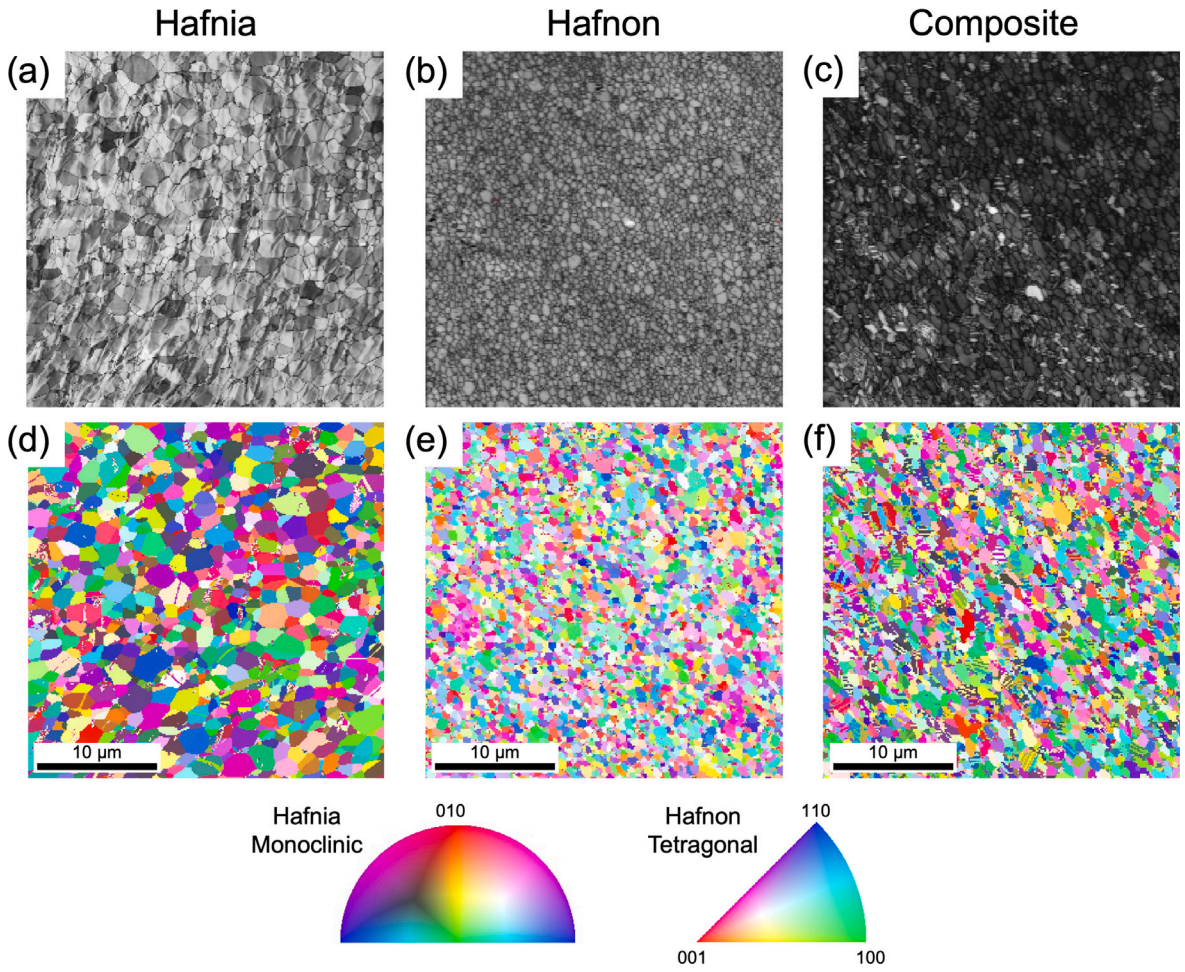

Fig. 6. EBSD maps collected at 10 keV with the DE-SEMCam for the three studied material systems: (a,d) hafnia; (b,e) hafnon; (c,f) hafnia/hafnon composite. (a-c) DI image quality maps (algorithmic description here [75]). (d-f) IPF color-coded maps obtained using the DI approach.

often 180° (Table A.4). One must consider the 11th most prevalent variant to obtain a slightly different value (179.67°). Consequently, the disorientations exceeding 176° emerge from PS variants, compounded by random indexing errors centered about 180°. An example of an ambiguous orientation is illustrated in the EBSP in Fig. 8, obtained from a pixel located within the red grain (180° disorientation) indicated by the white arrow in Fig. 7b. Comparing the HI- and DI-derived solutions reveals that the 180° discrepancy arises from the most likely PS variant (#1 in Table A.4) since the pattern flips about the (2 0 2) plane. The histograms in Fig. 7c and 7d show that at 5 keV and 10 keV, at least 13.8% and 4.5% of the disorientations are attributable to the PS variants, respectively. Generally, the comparison of the disorientation histograms underscores the lower accuracy of HI at low accelerating voltages.

Similar comparisons using hafnon (Fig. 9a,b) reveal that 81.5% of disorientations are below 20°, which arise from small errors centered around correct solutions; the remaining 18.5% of disorientations correspond to random indexing errors constrained by the Mackenzie distribution [76]). Interestingly, the number fraction of pixels with disorientation angles near 180° is zero, revealing that both indexing approaches robustly resolve tetragonal hafnon PS variants (see Table A.4). Fig. 9c shows the composite phase maps obtained by DI and HI; point-to-point comparisons in Fig. 9d reveal that DI and HI diverge in predicted phases 13% of the time (black pixels), notwithstanding compound error from orientation indexing.

4. Discussion

The sensitivity of the direct electron detector opens up many exciting opportunities to exploit small beam interaction volumes to resolve micron-scale grains and sub-grain features on lengthscales that typically fall between those accessible by conventional (phosphor-based) EBSD and transmission Kikuchi diffraction (TKD) [77]. Notable opportunities include characterizing epitaxially strained twinned ceramic films [78], shape memory ceramics comprising multiple sub-grain phase domains [67], and highly deformed nano-grained metals [79]. The low electron doses will also help mitigate surface charging, contamination, radiolysis, and heating, the last of which represents a major barrier to obtaining high resolution maps of heat-sensitive ceramic glasses [80].

The direct detection EBSD system also offers new capabilities in adjusting geometric parameters during pattern acquisition, since eliminating the phosphor screen and coupled optics effectively reduces the sensor size. As one example, a direct detector system enables pattern acquisition at 0° sample tilt [81], providing opportunities for *in situ* experiments, including imaging during thermo-mechanical loading. Similarly, several geometric parameters can be fine-tuned to achieve optimal imaging conditions for low symmetry crystals; these are cases in which it is crucial to capture a sufficient number of Kikuchi bands, zone axes, and higher-order diffraction information. (One can change the camera tilt, α, and the sample-to-detector distance L by moving

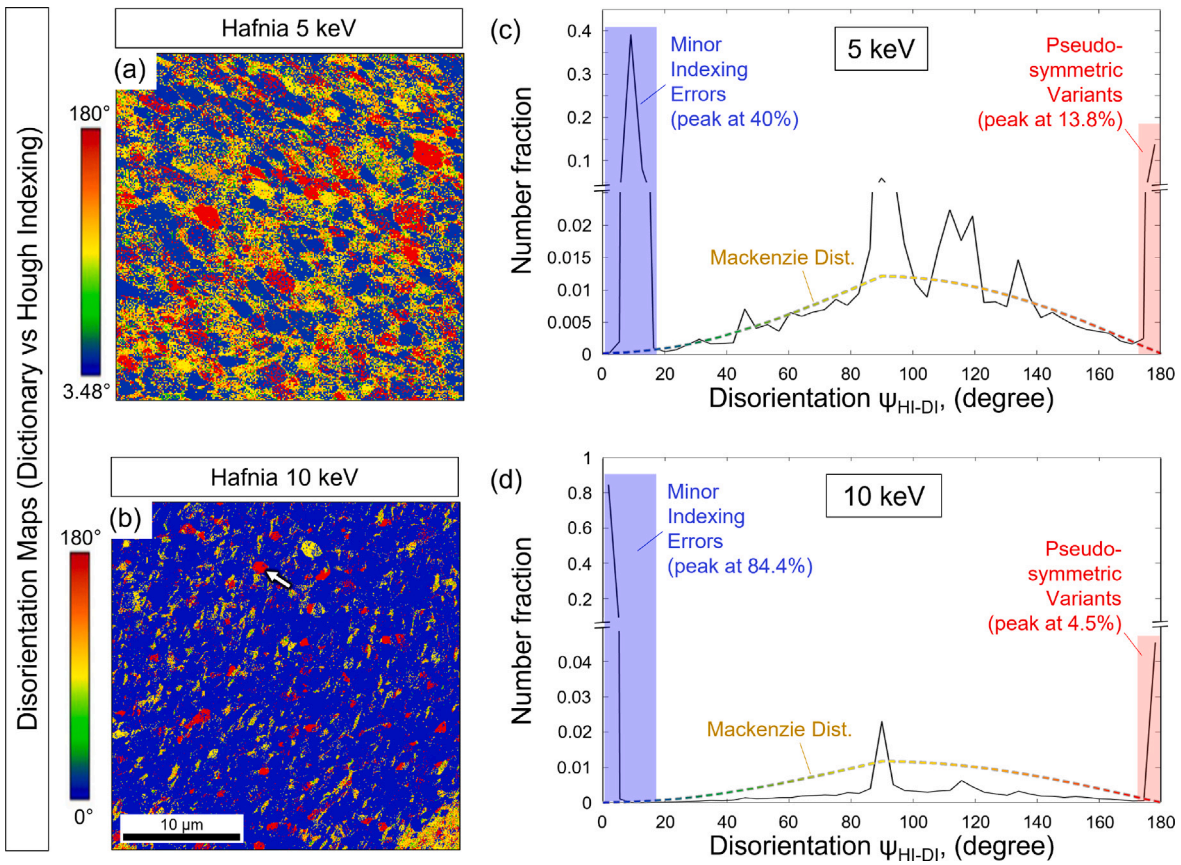

Fig. 7. (a,b) Point-to-point disorientation comparison between HI and DI solutions for the hafnia maps collected at 5 keV and 10 keV in Fig. 5a,b. (c,d) Corresponding disorientation histograms ranging from 0° to 180° suggesting several sources of discrepancies between indexing solutions. The bin size used is 50.

the detector along an insertion axis σ, at an adjustable angle β - see Fig. 2a). In the present work, since both hafnia and hafnon exhibit relatively few zone axes and strongly diffracting planes, larger solid angles (i.e. more diffraction space coverage, shorter detector distances) led to better indexing. Having more diffraction space coverage using shorter detector distances is especially important at lower accelerating voltages (e.g. 5 keV), as indexing accuracy improves. However, at longer detector distances, the rich diffraction information could prove useful in multiple research applications including dislocation network imaging and density estimation using pattern sharpness [82,83] and HR-EBSD for strain analysis [3,84].

The direct detector naturally complements new, precise indexing algorithms (e.g. DI and spherical indexing, SI [54]) that, unlike HI, leverage all of the rich higher-order diffraction information in EBSPs. In the present work, HI-related errors were largely attributable to how the algorithm relies only on geometric relationships between primary Kikuchi bands (and their associated fitting errors likely due to band broadening at low beam energies). For low symmetry materials in particular, HI may require sampling more of reciprocal space compared to that required for DI.

The direct detection EBSD-DI workflow also addresses longstanding issues in indexing low symmetry materials that exhibit multiple PS variants. It is striking that for hafnia at 5 keV, HI improperly indexed at least 13.8% of the 180° PS variant points (Fig. 7c). We suspect that 13.8% represents a lower bound to the error, since the yellow data in Fig. 7a,b –corresponding to 90° peak in Fig. 7(c)– are likely also PS variants given their presence across entire grains. By increasing the accelerating voltage to 10 keV, the area fraction of PS variants decreases to 4.5%, which may be due to the narrower bands (reducing band overlap) coupled with more backscatter electron yield (stronger signal). Both factors accentuate higher-order diffraction information, which has been shown to be critical for differentiating between PS variants that only differ by subtle features [5,6].

5. Conclusions

In the present work, we show that the combination of a direct electron detector and dictionary indexing enable the crystallographic mapping of micron-scale grain structures in low symmetry, charge-sensitive ceramics. To our knowledge, the EBSD maps of hafnia, hafnon, and hafnia/hafnon composites are the first to be reported. More broadly, the workflow presents a powerful new path to characterize many materials historically unsuited for EBSD. The key findings are as follows.

- The direct electron detector captures significantly better EBSPs at low beam energies (5–10 keV) and low currents (1.6–3.2 nA) compared to an indirect phosphor-coupled detector, at up to 10x shorter exposure times. These low-dose beam conditions mitigate surface charge accumulation on insulating, cracked samples.
- Since the direct detector facilitates small electron beam interaction volumes and thus small step sizes, high resolution orientation maps are obtainable. The maps reveal fine twin boundaries within hafnia grains and show that the composites contain about three times as many twins as the monoliths (~37% and ~11% of grain boundaries, respectively).
- At low accelerating voltages dictionary indexing performs better than Hough indexing because it considers the entirety of the diffraction information in a pattern (across all pixels) and thus exploits higher-order diffraction information.
- Errors in Hough indexing of hafnia maps are considerable and vary with accelerating voltage. They are estimated to be at least 13.8% at 5keV and 4.5% at 10 keV. These errors are ascribed to pseudo-symmetric variants.

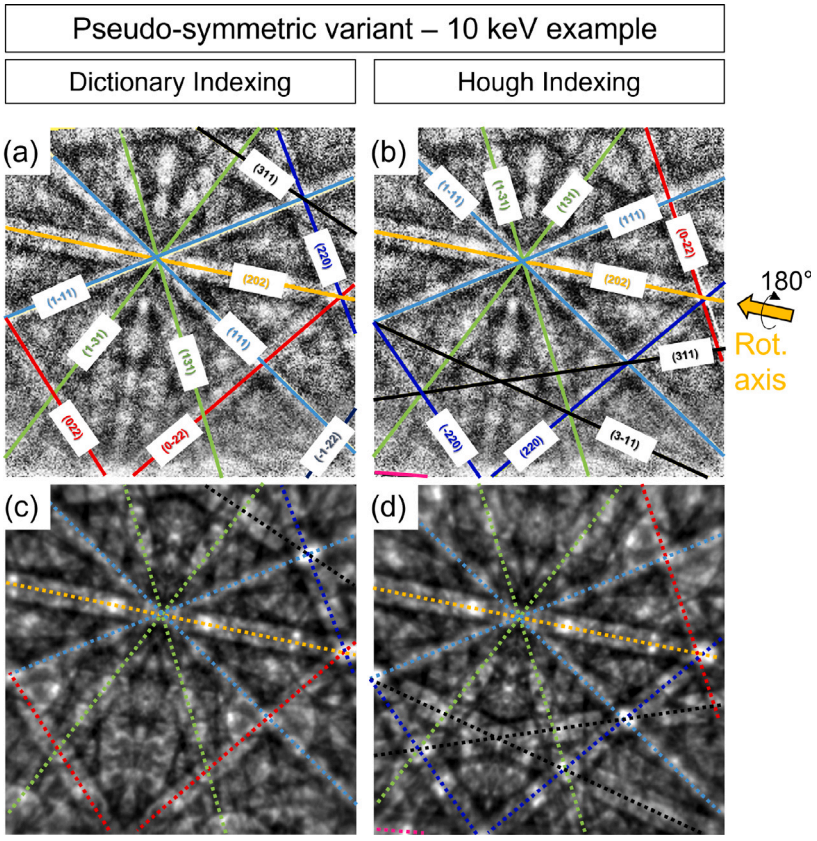

Fig. 8. EBSP extracted from a pixel within the red-colored grain (180° disorientation value) indicated by the white arrow in Fig. 7b, indexed using DI (a) and HI (b). The comparison reveals an erroneous pattern flip around the (202) plane for the HI result. Simulated patterns for the DI and HI solution are illustrated in panel (c) and (d), respectively.

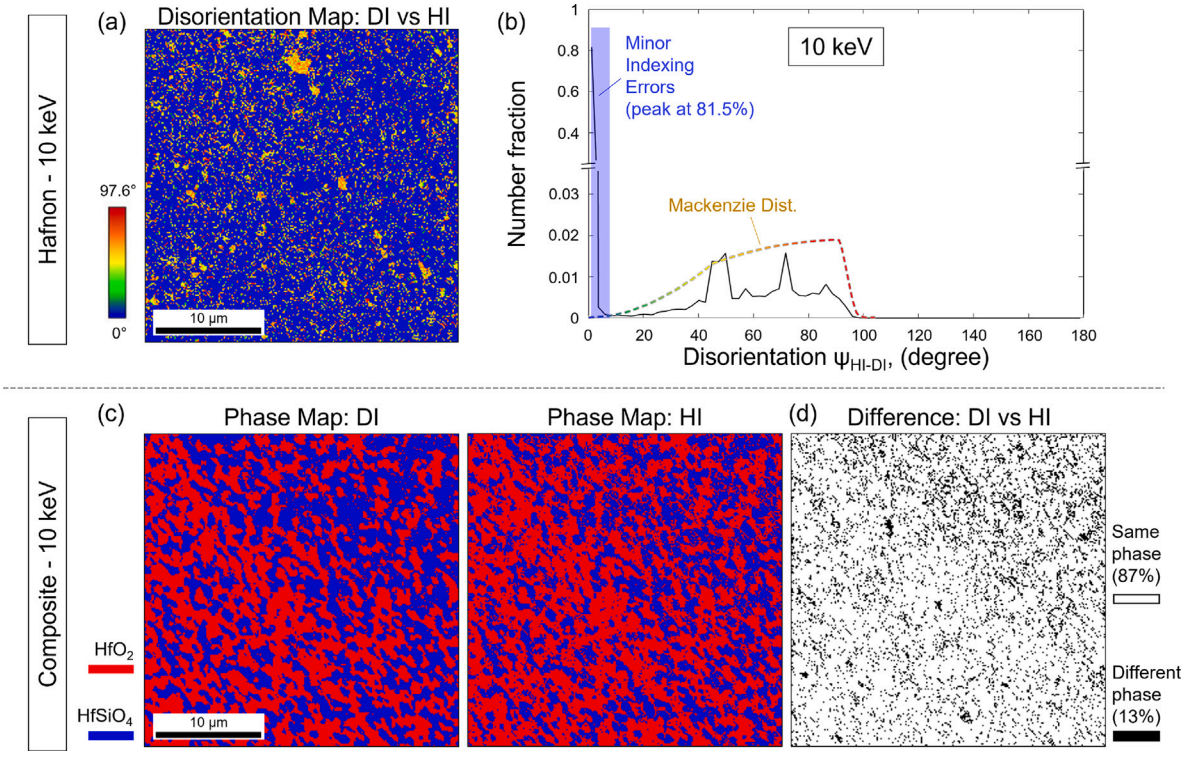

Fig. 9. Comparisons of HI and DI solutions for hafnon and hafnia/hafnon composites, collected using the DE-SEMCam. (a) Point-to-point disorientation map for hafnon collected at 10 keV and (b) the corresponding distribution of disorientation angles. The bin size used is 50. (c) Composite phase maps (also 10 keV) obtained from DI (left) and HI (center), with discrepancies shown in the map in (d).

Table A.1
Parameter used for Hough Indexing.

Software	Type	Pattern size	Theta step	Rho fraction	Max band count
OIM v9	Classic	96	1°	88	10

Convolution mask	Min peak magnitude	Min peak distance	Symmetry	Vertical bias
9 × 9	5	15	50	0

Table A.2
Detection parameters for Hafnia EBSPs in Fig. 4.

Detector/Technology	EBSP	keV	nA	Fps	# Frames per EBSP	Exposure (ms)	Gain	Bin	Dose ($\times 10^9 e^-$)
TSL/EDAX (Indirect)	Fig. 4a	5	14	2	1	500	847	2x	44
Phosphor-coupled	Fig. 4b	10	12	50	1	20	847	2x	1.5
DE-SEMCam (Direct)	Fig. 4c	5	3.2	15	1	67	–	2x	1.3
CMOS MAPS	Fig. 4d	10	1.6	50	1	20	–	2x	0.2
	Fig. 4e	5	3.2	55	220	4000	–	2x	80
	Fig. 4f	10	1.6	55	220	4000	–	2x	40

Detector/Technology	EBSP	Camera pxl	Camera pxl (processed&displayed)	Camera tilt	WD (mm)	L (mm)
TSL/EDAX (Indirect)	Fig. 4a	320 × 240	240 × 240	10°	10	26.717
Phosphor-coupled	Fig. 4b	320 × 240	240 × 240	10°	10	26.717
DE-SEMCam (Direct)	Fig. 4c	2048 × 2048	256 × 256	10.1°	8	24.046
CMOS MAPS	Fig. 4d	2048 × 2048	256 × 256	10.1°	13	23.080
	Fig. 4e	2048 × 2048	256 × 256	10.1°	11	30.620
	Fig. 4f	2048 × 2048	256 × 256	10.1°	11	30.590

- Phase identification in the composite maps is improved by ~13% when using dictionary indexing compared to Hough indexing.

CRediT authorship contribution statement

Nicolò M. Della Ventura: Writing – original draft, Visualization, Software, Methodology, Investigation, Formal analysis, Data curation. **Andrew R. Ericks:** Writing – original draft, Visualization, Software, Methodology, Investigation, Formal analysis, Data curation. **McLean P. Echlin:** Writing – original draft, Visualization, Software, Methodology, Investigation, Formal analysis, Data curation. **Kalani Moore:** Writing – review & editing, Software, Investigation, Formal analysis, Data curation. **Tresa M. Pollock:** Writing – review & editing, Supervision, Resources, Project administration, Methodology, Funding acquisition, Conceptualization. **Matthew R. Begley:** Writing – review & editing, Supervision, Resources, Project administration, Methodology, Funding acquisition, Conceptualization. **Frank W. Zok:** Writing – review & editing, Supervision, Resources, Project administration, Methodology, Funding acquisition, Conceptualization. **Marc De Graef:** Writing – review & editing, Visualization, Software, Methodology, Investigation, Formal analysis, Data curation. **Daniel S. Gianola:** Writing – review & editing, Supervision, Resources, Project administration, Methodology, Funding acquisition, Conceptualization.

Declaration of competing interest

The authors declare that they have no known competing financial interests or personal relationships that could have appeared to influence the work reported in this paper.

Acknowledgments

This research was supported by funds from the UC National Laboratory Fees Research Program of the University of California, USA, Grant Number L22CR4520, and from the Army Research Laboratory, USA accomplished under Cooperative Agreement Number W911NF-22-2-0121. The views and conclusions contained in this document are those of the authors and should not be interpreted as representing the official policies, either expressed or implied, of the Army Research Laboratory or the U.S. Government. The U.S. Government is authorized to reproduce and distribute reprints for Government purposes notwithstanding any copyright notation herein. Direct Electron's work in this publication was supported by the National Institute of Mental Health (NIMH) of the National Institutes of Health (NIH), USA under award number 1R44MH125687. The authors also acknowledge the NSF MRI instrumentation grant No. 2117843. The research reported here made use of the shared facilities of the Materials Research Science and Engineering Center (MRSEC) at UC Santa Barbara: NSF DMR–2308708. The UC Santa Barbara MRSEC is a member of the Materials Research Facilities Network (www.mrfn.org). MDG acknowledges financial support from a National Science Foundation, USA grant (DMR-2203378), use of the computational resources of the Materials Characterization Facility at Carnegie Mellon University, USA supported by grant MCF-677785, as well as support from the John and Claire Bertucci Distinguished Professorship in Engineering.

Appendix

See Tables A.1–A.4.

Appendix B. Supplementary data

Supplementary material related to this article can be found online at https://doi.org/10.1016/j.ultramic.2024.114079.

Data availability

Data will be made available on request.

Table A.3
Detection parameters for EBSD scans shown in Figs. 5, 6, 7, and 9.

TSL/EDAX - Sample	keV	nA	Fps	Gain	Scan size (pts)	Step size (nm)	Area (μm²)	Camera tilt
Hafnia	5	14	2	847	40 × 40	125	5 × 5	10°
Hafnia	10	12	50	847	240 × 240	125	30 × 30	10°
DE-SEMCam - Sample								
Hafnia	5	3.2	15	–	240 × 240	125	30 × 30	10.1°
Hafnia	10	1.6	50	–	240 × 240	125	30 × 30	10.1°
Hafnon	10	13	110	–	240 × 240	125	30 × 30	10.1°
Composite	10	13	110	–	240 × 240	125	30 × 30	10.1°

TSL/EDAX - Sample	WD (mm)	Bin	Camera pxl (processed)	L (mm)	Solid angle	PC (x*, y*, z*)
Hafnia	10	2x	240 × 240	26.717	~62°	0.4906, 0.7678, 0.8246
Hafnia	10	2x	240 × 240	26.717	~62°	0.4906, 0.7678, 0.8246
DE-SEMCam - Sample						PC (x*, y*, z*)
Hafnia	8	2x	256 × 256	24.046	~58°	0.5176, 0.7057, 0.9032
Hafnia	13	2x	256 × 256	23.080	~60°	0.5132, 0.4517, 0.8669
Hafnon	9.3	2x	256 × 256	25.702	~54°	0.5068, 0.5321, 0.9654
Composite	10	2x	256 × 256	25.175	~56°	0.4763, 0.4788, 0.9456

Table A.4
List of possible pseudo-symmetries obtained using OIM Analysis v9 software from the master pattern at 10 keV of each phase when auto-correlated with itself. The maximum auto-correlation value is 100.

Master pattern	#	Auto-correlation	Angle	Direction	Plane
HfO_2 with HfO_2	1	31.93	180.00°	⟨12 0 11⟩	(1 0 1)
	2	23.78	180.00°	⟨0 0 1⟩	(−1 0 6)
	3	16.99	180.00°	⟨1 0 6⟩	(0 0 1)
	4	16.84	180.00°	⟨2 0 3⟩	(1 0 2)
	5	14.02	180.00°	⟨2 −4 3⟩	(5 −14 10)
	6	14.02	180.00°	⟨2 4 3⟩	(5 14 10)
	7	13.35	180.00°	⟨0 1 1⟩	(−2 12 13)
	8	13.35	180.00°	⟨0 −1 1⟩	(−2 −12 13)
	9	13.00	180.00°	⟨−1 −1 1⟩	(−11 −10 12)
	10	13.00	180.00°	⟨−1 1 1⟩	(−11 10 12)
	11	12.94	179.67°	⟨−3 −7 3⟩	(−1 −2 1)
$HfSiO_4$ with $HfSiO_4$	1	23.47	180.00°	⟨2 0 1⟩	(5 0 2)
	2	23.47	180.00°	⟨2 0 5⟩	(1 0 2)
	3	23.44	180.00°	⟨0 2 1⟩	(0 5 2)
	4	23.44	180.00°	⟨0 2 5⟩	(0 1 2)
	5	18.87	180.00°	⟨0 2 3⟩	(0 4 5)
	6	18.87	180.00°	⟨0 5 4⟩	(0 3 2)
	7	18.83	180.00°	⟨5 0 4⟩	(3 0 2)
	8	18.83	180.00°	⟨2 0 3⟩	(4 0 5)
	9	18.52	180.00°	⟨2 1 0⟩	(2 1 0)
	10	18.52	180.00°	⟨3 1 0⟩	(3 1 0)
	11	12.88	180.00°	⟨0 1 4⟩	(0 1 3)

References

[1] A.J. Schwartz, M. Kumar, B.L. Adams, D.P. Field, Electron Backscatter Diffraction in Materials Science, Springer US, 2009, http://dx.doi.org/10.1007/978-0-387-88136-2.

[2] S.J. Dillon, G.S. Rohrer, Mechanism for the development of anisotropic grain boundary character distributions during normal grain growth, Acta Mater. 57 (1) (2009) 1–7, http://dx.doi.org/10.1016/j.actamat.2008.08.062.

[3] A.J. Wilkinson, D. Randman, Determination of elastic strain fields and geometrically necessary dislocation distributions near nanoindents using electron back scatter diffraction, Phil. Mag. 90 (9) (2010) 1159–1177, http://dx.doi.org/10.1080/14786430903304145.

[4] P. Cordier, S. Demouchy, B. Beausir, V. Taupin, F. Barou, C. Fressengeas, Disclinations provide the missing mechanism for deforming olivine-rich rocks in the mantle, Nature 507 (7490) (2014) 51–56, http://dx.doi.org/10.1038/nature13043.

[5] W. Lenthe, S. Singh, M. De Graef, Prediction of potential pseudo-symmetry issues in the indexing of electron backscatter diffraction patterns, J. Appl. Crystallogr. 52 (5) (2019) 1157–1168, http://dx.doi.org/10.1107/s1600576719011233.

[6] E.L. Pang, C.A. Schuh, Crystal orientation and detector distance effects on resolving pseudosymmetry by electron backscatter diffraction, J. Appl. Crystallogr. 54 (2) (2021) 513–522, http://dx.doi.org/10.1107/s1600576721001229.

[7] B. Jackson, D. Fullwood, J. Christensen, S. Wright, Resolving pseudosymmetry in γ-TiAl using cross-correlation electron backscatter diffraction with dynamically simulated reference patterns, J. Appl. Crystallogr. 51 (3) (2018) 655–669, http://dx.doi.org/10.1107/s1600576718003849.

[8] R.F. Cook, B.R. Lawn, C.J. Fairbanks, Microstructure-strength properties in ceramics: I, effect of crack size on toughness, J. Amer. Ceram. Soc. 68 (11) (1985) 604–615, http://dx.doi.org/10.1111/j.1151-2916.1985.tb16163.x.

[9] M.V. Swain, R-curve behavior in a polycrystalline alumina material, J. Mater. Sci. Lett. 5 (1986) 1313–1315, http://dx.doi.org/10.1007/BF01729403.

[10] G. Vekinis, M. Ashby, P. Beaumont, R-curve behaviour of Al_2O_3 ceramics, Acta Metall. Mater. 38 (6) (1990) 1151–1162, http://dx.doi.org/10.1016/0956-7151(90)90188-M.

[11] R.W. Rice, S.W. Freiman, P.F. Becher, Grain-size dependence of fracture energy in ceramics: I, experiment, J. Am. Ceram. Soc. 64 (6) (1981) 345–350, http://dx.doi.org/10.1111/j.1151-2916.1981.tb10300.x.

[12] A.F. Bower, M. Ortiz, The influence of grain size on the toughness of monolithic ceramics, J. Eng. Mater. Tech. 115 (3) (1993) 228–236, http://dx.doi.org/10.1115/1.2904212.

[13] A.B. Peters, D. Zhang, S. Chen, C. Ott, C. Oses, S. Curtarolo, I. McCue, T. Pollock, S.E. Prameela, Materials design for hypersonics, 2023, http://dx.doi.org/10.48550/ARXIV.2309.04053, URL https://arxiv.org/abs/2309.04053.

[14] J. Zhang, X. Ke, G. Gou, J. Seidel, B. Xiang, P. Yu, W.-I. Liang, A.M. Minor, Y. hao Chu, G.V. Tendeloo, X. Ren, R. Ramesh, A nanoscale shape memory oxide, Nature Commun. 4 (2768) (2013).

[15] M. Asle Zaeem, N. Zhang, M. Mamivand, A review of computational modeling techniques in study and design of shape memory ceramics, Comput. Mater. Sci. 160 (2019) 120–136, http://dx.doi.org/10.1016/j.commatsci.2018.12.062.

[16] A. Lai, Z. Du, C.L. Gan, C.A. Schuh, Shape memory and superelastic ceramics at small scales, Science 341 (6153) (2013) 1505–1508, http://dx.doi.org/10.1126/science.1239745.

[17] E.L. Pang, G.B. Olson, C.A. Schuh, Low-hysteresis shape-memory ceramics designed by multimode modelling, Nature 610 (2022) 491–495, http://dx.doi.org/10.1038/s41586-022-05210-1.

[18] G. Qian, Y. Zhang, L. Li, R. Zhang, J. Xu, Z. Cheng, S. Xie, H. Wang, Q. Rao, Y. He, Y. Shen, L. Chen, M. Tang, Z.-F. Ma, Single-crystal nickel-rich layered-oxide battery cathode materials: synthesis, electrochemistry, and intra-granular fracture, Energy Storage Mater. 27 (2020) 140–149, http://dx.doi.org/10.1016/j.ensm.2020.01.027.

[19] H.H. Sun, H.-H. Ryu, U.-H. Kim, J.A. Weeks, A. Heller, Y.-K. Sun, C.B. Mullins, Beyond doping and coating: prospective strategies for stable high-capacity layered Ni-rich cathodes, ACS Energy Lett. 5 (4) (2020) 1136–1146, http://dx.doi.org/10.1021/acsenergylett.0c00191.

[20] H.-T. Chung, B.-C. Shin, H.-G. Kim, Grain-size dependence of electrically induced microcracking in ferroelectric ceramics, J. Amer. Ceram. Soc. 72 (2) (1989) 327–329, http://dx.doi.org/10.1111/j.1151-2916.1989.tb06127.x.

[21] X. Tan, Z. Xu, J.K. Shang, In situ transmission electron microscopy observations of electric-field-induced domain switching and microcracking in ferroelectric ceramics, Mater. Sci. Eng. A 314 (1) (2001) 157–161, http://dx.doi.org/10.1016/S0921-5093(00)01911-0.

[22] M. Terheci, Grain boundary and testing procedure: a new approach to the tribology of alumina materials, Wear 211 (2) (1997) 289–301, http://dx.doi.org/10.1016/S0043-1648(07)00133-0.

[23] A.K. Mukhopadhyay, M. Yiu-Wing, Grain size effect on abrasive wear mechanisms in alumina ceramics, Wear 162–164 (1993) 258–268, http://dx.doi.org/10.1016/0043-1648(93)90508-J.

[24] W.R. Buessem, N.R. Thielke, R.V. Sarakauskas, Thermal expansion hysteresis of aluminum titanate, Ceram. Age 60 (5) (1952) 38–40.

[25] E.A. Bush, F.A. Hummel, High-temperature mechanical properties of ceramic materials: I, magnesium dititanate, J. Amer. Ceram. Soc. 41 (6) (1958) 189–195, http://dx.doi.org/10.1111/j.1151-2916.1958.tb13539.x.

[26] E.A. Bush, F.A. Hummel, High-temperature mechanical properties of ceramic materials: II, beta-eucryptite, J. Amer. Ceram. Soc. 42 (8) (1959) 388–391, http://dx.doi.org/10.1111/j.1151-2916.1959.tb13597.x.

[27] H.P. Kirchner, R.M. Gruver, Strength-anisotropy-grain size relations in ceramic oxides, J. Amer. Ceram. Soc. 53 (5) (1970) 232–236, http://dx.doi.org/10.1111/j.1151-2916.1970.tb12083.x.

[28] H.J. Siebeneck, D.P.H. Hasselman, J.J. Cleveland, R.C. Bradt, Effect of microcracking on the thermal diffusivity of Fe_2TiO_5, J. Amer. Ceram. Soc. 59 (5–6) (1976) 241–244, http://dx.doi.org/10.1111/j.1151-2916.1976.tb10944.x.

[29] B.L.A. Adam J. Schwartz, Electron Backscatter Diffraction in Materials Science, Springer US, 2000, http://dx.doi.org/10.1007/978-1-4757-3205-4.

[30] D. Zhang, Y. Zhu, L. Liu, X. Ying, C.-E. Hsiung, R. Sougrat, K. Li, Y. Han, Atomic-resolution transmission electron microscopy of electron beam–sensitive crystalline materials, Science 359 (6376) (2018) 675–679, http://dx.doi.org/10.1126/science.aao0865.

[31] X. Chen, Z. Wang, Investigating chemical and structural instabilities of lead halide perovskite induced by electron beam irradiation, Micron 116 (2019) 73–79, http://dx.doi.org/10.1016/j.micron.2018.09.010.

[32] F. Wang, M.P. Echlin, A.A. Taylor, J. Shin, B. Bammes, B.D. Levin, M. De Graef, T.M. Pollock, D.S. Gianola, Electron backscattered diffraction using a new monolithic direct detector: High resolution and fast acquisition, Ultramicroscopy 220 (2021) 113160, http://dx.doi.org/10.1016/j.ultramic.2020.113160.

[33] A.J. Wilkinson, G. Moldovan, T.B. Britton, A. Bewick, R. Clough, A.I. Kirkland, Direct detection of electron backscatter diffraction patterns, Phys. Rev. Lett. 111 (6) (2013) http://dx.doi.org/10.1103/physrevlett.111.065506.

[34] S. Vespucci, A. Winkelmann, G. Naresh-Kumar, K.P. Mingard, D. Maneuski, P.R. Edwards, A.P. Day, V. O'Shea, C. Trager-Cowan, Digital direct electron imaging of energy-filtered electron backscatter diffraction patterns, Phys. Rev. B 92 (20) (2015) 205301.

[35] K.P. Mingard, M. Stewart, M.G. Gee, S. Vespucci, C. Trager-Cowan, Practical application of direct electron detectors to EBSD mapping in 2D and 3D, Ultramicroscopy 184 (2018) 242–251, http://dx.doi.org/10.1016/j.ultramic.2017.09.008.

[36] S. Ueno, D. Jayaseelan, H. Kita, T. Ohji, H. Lin, Comparison of water vapor corrosion behaviors of $Ln_2Si_2O_7$ (Ln=Yb and Lu) and $ASiO_4$ (A=Ti, Zr and Hf) EBCs, Key Eng. Mater. 317 (2006) 557–560.

[37] M. Winter, D. Clarke, Thermal conductivity of yttria-stabilized zirconia–hafnia solid solutions, Acta Mater. 54 (18) (2006) 5051–5059.

[38] R. Anton, V. Leisner, P. Watermeyer, M. Engstler, U. Schulz, Hafnia-doped silicon bond coats manufactured by PVD for SiC/SiC CMCs, Acta Mater. 183 (2020) 471–483.

[39] B. Harder, Oxidation performance of Si-HfO_2 environmental barrier coating bond coats deposited via plasma spray-physical vapor deposition, Surf. Coat. Technol. 384 (2020) 125311.

[40] J. Deijkers, H. Wadley, Hafnium silicate formation during the reaction of β-cristobalite SiO_2 and monoclinic HfO_2 particles, J. Am. Ceram. Soc. 103 (9) (2020) 5400–5410.

[41] J. Deijkers, H. Wadley, A duplex bond coat approach to environmental barrier coating systems, Acta Mater. 217 (2021) 117167.

[42] C.S. Holgate, Y. Yang, C.G. Levi, Reactive crystallization in HfO_2 exposed to molten silicates, J. Eur. Ceram. Soc. 41 (11) (2021) 5686–5695, http://dx.doi.org/10.1016/j.jeurceramsoc.2021.03.025.

[43] A.R. Ericks, C.S. Holgate, A.A. Taylor, C.G. Levi, F.W. Zok, Interactions of hafnia/hafnon composites with molten silicate deposits, J. Eur. Ceram. Soc. 43 (12) (2023) 5359–5372, http://dx.doi.org/10.1016/j.jeurceramsoc.2023.04.058.

[44] R. Patil, E. Subbarao, Axial thermal expansion of ZrO_2 and HfO_2 in the range room temperature to 1400 °C, J. Appl. Crystallogr. 2 (6) (1969) 281–288.

[45] J.A. Kuszyk, R.C. Bradt, Influence of grain size on effects of thermal expansion anisotropy in $MgTi_2O_5$, Received January 25, 1973; revised copy received April 2, 1973, J. Amer. Ceram. Soc. 56 (8) (1973) 420–423, http://dx.doi.org/10.1111/j.1151-2916.1973.tb12714.x.

[46] J.J. Cleveland, R.C. Bradt, Grain size/microcracking relations for pseudobrookite oxides, Received March 10, 1978; revised copy received May 18, 1978., J. Amer. Ceram. Soc. 61 (11–12) (1978) 478–481, http://dx.doi.org/10.1111/j.1151-2916.1978.tb16121.x.

[47] S.L. Dole, O. Hunter Jr., F.W. Calderwood, D.J. Bray, Microcracking of monoclinic HfO_2, J. Amer. Ceram. Soc. 61 (11–12) (1978) 486–490, http://dx.doi.org/10.1111/j.1151-2916.1978.tb16123.x.

[48] G. Bayer, Thermal expansion of ABO_4-compounds with zircon-and scheelite structures, J. Less Common Met. 26 (1) (1972) 255–262.

[49] E. Subbarao, D. Agrawal, H. McKinstry, C. Sallese, R. Roy, Thermal expansion of compounds of zircon structure, J. Am. Ceram. Soc. 73 (5) (1990) 1246–1252.

[50] S.I. Wright, B.L. Adams, Automatic analysis of electron backscatter diffraction patterns, Metall. Trans. A 23 (3) (1992) 759–767, http://dx.doi.org/10.1007/bf02675553.

[51] N. Krieger Lassen, D. Juul Jensen, K. Conradsen, Image processing procedures for analysis of electron back scattering patterns, Scanning Microsc. 6 (1) (1992) 7.

[52] P.T. Pinard, M. Lagacé, P. Hovington, D. Thibault, R. Gauvin, An open-source engine for the processing of electron backscatter patterns: EBSD-image, Microsc. Microanal. 17 (3) (2011) 374–385, http://dx.doi.org/10.1017/s1431927611000456.

[53] T.B. Britton, V.S. Tong, J. Hickey, A. Foden, A.J. Wilkinson, AstroEBSD: exploring new space in pattern indexing with methods launched from an astronomical approach, J. Appl. Crystallogr. 51 (6) (2018) 1525–1534, http://dx.doi.org/10.1107/s1600576718010373.

[54] W. Lenthe, S. Singh, M.D. Graef, A spherical harmonic transform approach to the indexing of electron back-scattered diffraction patterns, Ultramicroscopy 207 (2019) 112841, http://dx.doi.org/10.1016/j.ultramic.2019.112841.

[55] Y.H. Chen, S.U. Park, D. Wei, G. Newstadt, M.A. Jackson, J.P. Simmons, M. De Graef, A.O. Hero, A dictionary approach to electron backscatter diffraction indexing, Microsc. Microanal. 21 (3) (2015) 739–752, http://dx.doi.org/10.1017/s1431927615000756.

[56] A.J. Wilkinson, D.M. Collins, Y. Zayachuk, R. Korla, A. Vilalta-Clemente, Applications of multivariate statistical methods and simulation libraries to analysis of electron backscatter diffraction and transmission Kikuchi diffraction datasets, Ultramicroscopy 196 (2019) 88–98, http://dx.doi.org/10.1016/j.ultramic.2018.09.011.

[57] A. Foden, D. Collins, A. Wilkinson, T. Britton, Indexing electron backscatter diffraction patterns with a refined template matching approach, Ultramicroscopy 207 (2019) 112845, http://dx.doi.org/10.1016/j.ultramic.2019.112845.

[58] R. Hielscher, F. Bartel, T.B. Britton, Gazing at crystal balls: Electron backscatter diffraction pattern analysis and cross correlation on the sphere, Ultramicroscopy 207 (2019) 112836, http://dx.doi.org/10.1016/j.ultramic.2019.112836.

[59] M.A. Jackson, E. Pascal, M. De Graef, Dictionary indexing of electron back-scatter diffraction patterns: a hands-on tutorial, Integr. Mater. Manuf. Innov. 8 (2) (2019) 226–246, http://dx.doi.org/10.1007/s40192-019-00137-4.

[60] A. Winkelmann, G. Nolze, Point-group sensitive orientation mapping of non-centrosymmetric crystals, Appl. Phys. Lett. 106 (7) (2015) http://dx.doi.org/10.1063/1.4907938.

[61] G. Nolze, M. Jürgens, J. Olbricht, A. Winkelmann, Improving the precision of orientation measurements from technical materials via EBSD pattern matching, Acta Mater. 159 (2018) 408–415, http://dx.doi.org/10.1016/j.actamat.2018.08.028.

[62] D.J. Rowenhorst, P.G. Callahan, H.W. Ånes, Fast radon transforms for high-precision EBSD orientation determination using PyEBSDIndex, J. Appl. Crystallogr. 57 (1) (2024) 3–19, http://dx.doi.org/10.1107/s1600576723010221.

[63] E.L. Pang, P.M. Larsen, C.A. Schuh, Global optimization for accurate determination of EBSD pattern centers, Ultramicroscopy 209 (2020) 112876, http://dx.doi.org/10.1016/j.ultramic.2019.112876.

[64] D. Fullwood, M. Vaudin, C. Daniels, T. Ruggles, S.I. Wright, Validation of kinematically simulated pattern HR-EBSD for measuring absolute strains and lattice tetragonality, Mater. Charact. 107 (2015) 270–277, http://dx.doi.org/10.1016/j.matchar.2015.07.017.

[65] T. Tanaka, A.J. Wilkinson, Pattern matching analysis of electron backscatter diffraction patterns for pattern centre, crystal orientation and absolute elastic strain determination – accuracy and precision assessment, Ultramicroscopy 202 (2019) 87–99, http://dx.doi.org/10.1016/j.ultramic.2019.04.006.

[66] C. Zhu, C. Kurniawan, M. Ochsendorf, D. An, S. Zaefferer, M. De Graef, Orientation, pattern center refinement and deformation state extraction through global optimization algorithms, Ultramicroscopy 233 (2022) 113407, http://dx.doi.org/10.1016/j.ultramic.2021.113407.

[67] E.L. Pang, C.A. McCandler, C.A. Schuh, Reduced cracking in polycrystalline ZrO2-CeO2 shape-memory ceramics by meeting the cofactor conditions, Acta Mater. 177 (2019) 230–239, http://dx.doi.org/10.1016/j.actamat.2019.07.028.

[68] J. Garay, Current-activated, pressure-assisted densification of materials, Annu. Rev. Mater. Res. 40 (2010) 445–468.

[69] C373-18 Standard Test Methods for Determination of Water Absorption and Associated Properties by Vacuum Method for Pressed Ceramic Tiles and Glass Tiles and Boil Method for Extruded Ceramic Tiles and Non-tile Fired Ceramic Whiteware Products, ASTM International, 2018.

[70] M. De Graef, Emsoft-org/emsoft: Emsoft release 5.0.0 — zenodo.org, 2024, https://zenodo.org/record/3489720. (Accessed 20 February 2024).

[71] M. De Graef, GitHub - marcdegraef/emsoft: Public emsoft repository — github.com, 2024, http://github.com/marcdegraef/EMsoft. (Accessed 20 February 2024).

[72] S. Singh, M. De Graef, Orientation sampling for dictionary-based diffraction pattern indexing methods, Modelling Simul. Mater. Sci. Eng. 24 (8) (2016) 085013, http://dx.doi.org/10.1088/0965-0393/24/8/085013.

[73] S. Singh, M. De Graef, Dictionary indexing of electron channeling patterns, Microsc. Microanal. 23 (1) (2017) 1–10, http://dx.doi.org/10.1017/s1431927616012769.

[74] J. DeRonja, M. Nowell, S. Wright, J. Kacher, Generational assessment of EBSD detectors for cross-correlation-based analysis: From scintillators to direct detection, Ultramicroscopy 257 (2024) 113913, http://dx.doi.org/10.1016/j.ultramic.2023.113913.

[75] K. Marquardt, M. De Graef, S. Singh, H. Marquardt, A. Rosenthal, S. Koizuimi, Quantitative electron backscatter diffraction (EBSD) data analyses using the dictionary indexing (DI) approach: Overcoming indexing difficulties on geological materials, Am. Mineral. 102 (9) (2017) 1843–1855, http://dx.doi.org/10.2138/am-2017-6062.

[76] T. Francis, I. Chesser, S. Singh, E.A. Holm, M. De Graef, A geodesic octonion metric for grain boundaries, Acta Mater. 166 (2019) 135–147, http://dx.doi.org/10.1016/j.actamat.2018.12.034.

[77] G.C. Sneddon, P.W. Trimby, J.M. Cairney, Transmission Kikuchi diffraction in a scanning electron microscope: A review, Mater. Sci. Eng. R 110 (2016) 1–12, http://dx.doi.org/10.1016/j.mser.2016.10.001.

[78] L. Torrejón, E. Langenberg, C. Magén, Á. Larrea, J. Blasco, J. Santiso, P.A. Algarabel, J.A. Pardo, Growth and structural characterization of strained epitaxial $Hf_{0.5}Zr_{0.5}O_2$ thin films, Phys. Rev. Mater. 2 (2018) 013401, http://dx.doi.org/10.1103/PhysRevMaterials.2.013401.

[79] S. Singh, Y. Guo, B. Winiarski, T.L. Burnett, P.J. Withers, M. De Graef, High resolution low kV EBSD of heavily deformed and nanocrystalline aluminium by dictionary-based indexing, Sci. Rep. 8 (1) (2018) http://dx.doi.org/10.1038/s41598-018-29315-8.

[80] W. Wisniewski, G. Völksch, C. Rüssel, The degradation of EBSD-patterns as a tool to investigate surface crystallized glasses and to identify glassy surface layers, Ultramicroscopy 111 (12) (2011) 1712–1719, http://dx.doi.org/10.1016/j.ultramic.2011.09.008.

[81] A. Marshall, J. Holzer, P. Stejskal, C. Stephens, T. Vystavěl, M. Whiting, The EBSD spatial resolution of a timepix-based detector in a tilt-free geometry, Ultramicroscopy 226 (2021) 113294, http://dx.doi.org/10.1016/j.ultramic.2021.113294.

[82] F. Wang, J.-C. Stinville, M. Charpagne, M.P. Echlin, S.R. Agnew, T.M. Pollock, M.D. Graef, D.S. Gianola, Dislocation cells in additively manufactured metallic alloys characterized by electron backscatter diffraction pattern sharpness, Mater. Charact. 197 (2023) 112673, http://dx.doi.org/10.1016/j.matchar.2023.112673.

[83] C. Zhu, M. De Graef, EBSD pattern simulations for an interaction volume containing lattice defects, Ultramicroscopy 218 (2020) 113088, http://dx.doi.org/10.1016/j.ultramic.2020.113088.

[84] T.B. Britton, J.L.R. Hickey, Understanding deformation with high angular resolution electron backscatter diffraction (HR-EBSD), IOP Conf. Ser. Mater. Sci. Eng. 304 (2018) 012003, http://dx.doi.org/10.1088/1757-899x/304/1/012003.